AGU100 ADVANCING EARTH AND SPACE SCIENCE

JGR

Journal of Geophysical Research: Space Physics

RESEARCH ARTICLE
10.1029/2018JA025575

Key Points:
- Response of CO_2 in the Austral winter MLT to the 11-year solar cycle is presented
- Solar cycle response of CO_2 in the Austral winter MLT is driven by photochemistry and transport
- The residual circulation and eddy diffusion in the Austral winter lower thermosphere respond to the 11-year solar cycle

Correspondence to:
L. C. Chang,
loren@jupiter.ss.ncu.edu.tw

Citation:
Salinas, C. C. J. H., Chang, L. C., Liang, M.-C., Qian, L., Yue, J., Lee, J. N., et al. (2018). Solar cycle response of CO_2 over the austral winter mesosphere and lower thermosphere region. *Journal of Geophysical Research: Space Physics*, *123*, 7581–7597. https://doi.org/10.1029/2018JA025575

Received 11 APR 2018
Accepted 22 JUL 2018
Accepted article online 1 AUG 2018
Published online 3 SEP 2018

Solar Cycle Response of CO_2 Over the Austral Winter Mesosphere and Lower Thermosphere Region

Cornelius Csar Jude H. Salinas[1,2,3,4], Loren C. Chang[1,3,4], Mao-Chang Liang[1,5,6], Liying Qian[7], Jia Yue[8,9], Jae N. Lee[10], James Russell III[8], Martin Mlynczak[11], and Dong L. Wu[12]

[1]Taiwan International Graduate Program-Earth Systems Science, Academia Sinica, Taipei, Taiwan, [2]Department of Atmospheric Sciences, National Central University, Taoyuan City, Taiwan, [3]Center for Astronautical Physics and Engineering, National Central University, Taoyuan City, Taiwan, [4]Graduate Institute of Space Science, National Central University, Taoyuan City, Taiwan, [5]Graduate Institute of Astronomy, National Central University, Taoyuan City, Taiwan, [6]Institute of Earth Sciences, Academia Sinica, Taipei, Taiwan, [7]High Altitude Observatory, National Center for Atmospheric Research, Boulder, CO, USA, [8]Center for Atmospheric Sciences, Hampton University, Hampton, VA, USA, [9]ESSIC, University of Maryland, Baltimore, MD, USA, [10]Joint Center for Earth Systems Technology, University of Maryland, Baltimore County, MD, USA, [11]NASA Langley Research Center, Hampton, VA, USA, [12]NASA Goddard Space Flight Center, Greenbelt, MD, USA

Abstract This work uses Sounding of the Atmosphere using Broadband Emission Radiometry CO_2 data from 2002 to 2015 and Specified Dynamics-Whole Atmosphere Community Climate Model (SD-WACCM) outputs from 1979 to 2014 to show, for the first time, the solar cycle response of CO_2 in the Austral winter mesosphere and lower thermosphere region. Both Sounding of the Atmosphere using Broadband Emission Radiometry and SD-WACCM show that CO_2 experiences a decrease during solar maximum throughout the Austral winter mesosphere and lower thermosphere region. This work highlights the regions where CO_2 experiences its strongest and weakest solar cycle responses as modeled by SD-WACCM. The region with the strongest solar cycle response experiences around 5% reduction in CO_2 between solar maximum and solar minimum. The region with weakest solar cycle response experiences less than 1% reduction in CO_2 between solar maximum and solar minimum. It is shown that the region of the strongest CO_2 response is driven by photodissociation, downwelling, and reduced eddy diffusion. On the other hand, the region of the weakest CO_2 response is driven by the opposing effects of photodissociation and enhanced eddy diffusion. This is the first work to show that the solar cycle could affect the Austral winter lower thermosphere circulation and eddy diffusion processes. These anomalies in the lower thermospheric circulation and eddy diffusion are found to be related to the solar cycle response in the Austral winter mesosphere wave-mean flow dynamics. This work therefore concludes that the solar cycle affects lower thermospheric CO_2 via modulations of the lower thermospheric circulation and eddy diffusion processes.

1. Introduction

The ultraviolet (UV) and extreme UV (EUV) fluxes are known to vary with the 11-year solar cycle (SC) variation (Beig et al., 2008; Gray et al., 2010; Lean et al., 1997; Woods & Rottman, 1997). Specifically, the EUV fluxes vary by a factor of 2 or more with the 11-year SC (Lean et al., 1997). The UV fluxes vary by 3–10% depending on wavelength (Ermolli et al., 2013; Haberreiter et al., 2017). The SC modulation of UV is known to induce significant changes in stratospheric ozone because the photochemistry of ozone is predominantly driven by UV dissociative photons (Gray et al., 2009; Labitzke, 2003; McCormack & Hood, 1996; Randel & Wu, 2007; Shindell et al., 1999). Numerous modeling and observational studies have already identified some consistent SC responses in the stratosphere (~15 to ~50 km) during solstice (Chiodo et al., 2012; Hampson et al., 2005; Hampson et al., 2006; Keckhut et al., 2005; Kodera & Kuroda, 2002; Langematz et al., 2005; Marsh et al., 2007; Matthes et al., 2004; Schmidt et al., 2006; Schmidt & Brasseur, 2006; Shibata & Kodera, 2005; Tsutsui et al., 2009). They found that in early winter during solar maximum, stratospheric ozone increases, which then increases diabatic heating over the summer hemisphere and the equator. This strengthens the stratospheric westerly jet over the winter hemisphere. As winter progresses, this enhancement in the jet perturbs the wave-mean flow dynamics over the winter hemisphere. Specifically, this alters the propagation of planetary Rossby waves by refracting them poleward and downward. Consequently, the zonal-mean zonal wind anomalies move poleward and downward, causing an enhancement of the winter polar jet. This further

hinders breaking planetary waves from enhancing the winter residual circulation, which yields a net weakening of this winter cell. Numerous studies have then shown how these SC responses in the stratosphere affect the troposphere (Baldwin & Dunkerton, 2005; Lu et al., 2017a, 2017b; Matthes et al., 2006; Mitchell et al., 2015). A less explored topic is how the stratospheric SC response affects the residual circulation and diffusion processes in the mesosphere and lower thermosphere region (MLT region) during solstice.

The structure of the MLT region (~50 to ~110 km) is largely affected by gravity waves. Gravity waves are known to vertically propagate and are filtered by background zonal winds (e.g., polar jet). Only gravity waves whose phase velocity is opposite to the background zonal winds or whose speed is faster than the background zonal wind in the stratosphere and mesosphere are able to vertically propagate through these regions (Fritts & Alexander, 2003). In the mesopause, air density becomes too low such that gravity waves saturate and break. Breaking gravity waves deposit their momentum and heat into the background atmosphere. Because of this, the winter mesopause easterly jet is produced due to breaking easterly gravity waves, while the summer mesopause westerly jet is due to breaking westerly gravity waves. The Coriolis force then induces a summer-to-winter mesospheric residual circulation closed by adiabatic cooling over the summer mesopause and by adiabatic warming over the winter mesopause. Above the mesopause, the lower thermosphere also has a residual circulation albeit opposite in direction to the mesopause residual circulation (Qian et al., 2017; Smith et al., 2011). The lower thermospheric circulation is directed from the winter hemisphere to the summer hemisphere because the gravity waves that drive them are opposite in phase velocity direction to the gravity waves driving the mesopause.

Recent works started showing a possible SC response in the mesospheric residual circulation during solstice seasons and how it is initiated by the SC response of the stratosphere (Cullens et al., 2016; Gan et al., 2017; Hampson et al., 2005; Keckhut et al., 2005; Li et al., 2011). Kodera and Kuroda (2002) and Kodera et al. (2003) both reported on enhancements of the lower mesospheric winter subtropical jet during solar maximum period as a response to the strengthening of the stratospheric winter jet. Cullens et al. (2016) added that these responses in the zonal-mean zonal wind induce changes in gravity wave propagation, and consequently, the mesospheric residual circulation. Using the Whole Atmosphere Community Climate Model version 4 (WACCM4), they found that the enhanced winter mesospheric subtropical jet further reduces the westerly gravity waves, which then induces a net easterly anomaly in the mesosphere. This then enhances the poleward and downward residual circulation over the winter hemisphere. Gan et al. (2017) corroborated these results using temperature observations from the Sounding of the Atmosphere using Broadband Emission Radiometry (SABER) payload onboard the Thermosphere Ionosphere Mesosphere Energetics and Dynamics (TIMED) satellite and 30-year model outputs from the Extended Canadian Middle Atmosphere Model.

While there has been progress on understanding the SC response of the mesosphere, little is known on the SC response of the lower thermosphere (~90 to ~110 km). This is because the presence of another gravity wave-driven winter-to-summer residual circulation was shown only recently (Qian et al., 2017; Smith et al., 2011). This work aims to further advance our knowledge of the SC responses of the MLT region during solstice seasons. We will present and analyze the SC response of lower thermosphere phenomena driven by lower atmosphere processes for the first time. This work builds off of Qian et al. (2017) by also utilizing CO_2 as a tracer for MLT dynamics. CO_2 is primarily controlled by both advection and diffusion throughout the MLT region (LóPez-Puertas et al., 2000). This will also allow us to subsequently determine the effects of the SC on the transport of lower thermospheric CO_2. Determining how the SC affects the transport of CO_2 is important because it contributes significantly to the energy balance of the MLT region (Beig et al., 2008; Marsh, 2011). CO_2 is an important cooling agent throughout the MLT region (Mlynczak, 2000). Beig et al. (2008) gave a review on the SC response of the MLT region's temperature structure and pointed out that understanding the SC response of the MLT region's energy balance remains a challenge.

This work utilizes 13 years of CO_2 data from SABER onboard the TIMED satellite. This work starts by using SABER CO_2 to validate model outputs from the Specified Dynamics-WACCM (SD-WACCM). These model outputs will then be used to determine and explain the possible SC responses of CO_2 in the MLT region during solstice seasons. By exploring the SC response of CO_2 in the MLT region during solstice seasons, this work aims to show how the SC responses of wave-mean flow dynamics in the MLT region could possibly affect the advective and diffusive transport of CO_2 in the MLT region.

2. Methodology

2.1. Satellite Observations and SD-WACCM

This work utilizes CO_2 observations from the SABER instrument onboard the TIMED satellite (Rezac et al., 2015b; Russell III et al., 1999). All CO_2 profiles from February 2002 to December 2015 are used. These CO_2 observations are mostly reliable between the altitudes of 80 and 110 km (Rezac et al., 2015a). These CO_2 observations were first vertically interpolated onto SD-WACCM pressure levels. This vertical interpolation is acceptable because the CO_2 observations have a higher vertical resolution than SD-WACCM. The latitudinal coverage of SABER alternates between 53°S–82°N and 82°S–53°N because of the 60-day spacecraft yaw cycle (Russell III et al., 1999). Thus, this work will only use CO_2 profiles between 50°S and 50 N. Also, with an orbital period of 1.6 hr and a local time precession of 12 min per day, it takes 60 days to sample all latitudes with complete local time coverage. Thus, we binned the data into bimonthly 5° zonal means from 85°S to 85 N.

There are only day-time CO_2 profiles (Rezac et al., 2015b). There have not yet been reports on the tidal modulation of CO_2 profiles, so it is difficult to ascertain how this will affect our results. At the very least, previous works have shown that during solstice, the migrating semidiurnal tide is significant over the winter hemisphere poleward of 30° latitude (Pancheva et al., 2009; Zhang et al., 2006). Thus, for now this work just cautions on results involving SABER observations beyond 30° latitude. These SABER CO_2 observations also encompass only one solar-cycle. While this may not be enough to isolate robust signals of the SC responses of CO_2, it can be used to validate a model over the same time span. In this work, these observations are used to validate model outputs from SD-WACCM. SD-WACCM is a version of the Whole WACCM4 that is constrained by the Modern-Era Retrospective Analysis for Research and Applications (MERRA) Reanalysis data set (Marsh et al., 2013; Rienecker et al., 2011). The model extends from the surface to ~140 km but is nudged to MERRA below ~50 km. Constraining the model with MERRA below ~50 km ensures that the model is realistic from the surface to the stratosphere (Kunz et al., 2011). This thus allows us to determine the response of the MLT region to SC changes in the stratosphere. All monthly model outputs from 1979 to 2014 were used. The model runs started in 1979 because the earliest available MERRA data set is in 1979. For consistency with the observations, they were also binned to bimonthly zonal mean.

Comparisons with observations of temperature and trace species have already shown that SD-WACCM can simulate the summer-to-winter circulation up to the mesosphere. To model the MLT region, an accurate gravity wave parameterization is necessary. SD-WACCM utilizes the Lindzen-type gravity wave parameterization scheme (Lindzen, 1981). The gravity wave source and spectrum takes into account flow over topography, frontal systems, and convection (Richter et al., 2010). Garcia et al. (2014) improved the gravity wave parameterization by adjusting eddy diffusion coefficients in the model. Recently, Qian et al. (2017) showed good agreement with CO_2 observations from SABER for SD-WACCM to simulate the winter-to-summer circulation in the lower thermosphere. Since this circulation is important in lower thermospheric CO_2 variability, this allows us to use SD-WACCM in determining the SC response of the lower thermospheric residual circulation.

2.2. Chemical Tendency Analysis

A chemical tendency analysis using the continuity equations for CO_2 is performed to explain how the SC affects its concentration in the MLT region. This analysis is applied to the SD-WACCM outputs. In the transformed Eulerian mean (TEM) system, the continuity equation for a given zonal-mean of species concentration (in parts-per-million) $\overline{\mu}$ is given by

$$\frac{\partial \overline{\mu}}{\partial t} = -\frac{\overline{v}^*}{a}\frac{\partial \overline{\mu}}{\partial \phi} - \overline{w}^*\frac{\partial \overline{\mu}}{\partial z} + \overline{P} - \overline{L}\overline{\mu} + \overline{X}_K + \overline{X}_D \tag{1}$$

where t is time. ϕ is latitude. z is geopotential height. $\overline{P}$ is the zonal-mean chemical production rate. $\overline{L}$ is the zonal-mean chemical loss rate. $\overline{v}^*$ and $\overline{w}^*$ are the TEM meridional and vertical winds (hereafter referred together as the residual circulation). They are defined as

$$\overline{v}^* = \overline{v} - \frac{1}{\rho_0}\frac{\partial}{\partial z}\left(\rho_0 \frac{\overline{v'\theta'}}{\overline{\theta}_z}\right) \tag{2}$$

$$\overline{w}^* = \overline{w} + \frac{1}{a\cos\phi}\frac{\partial}{\partial \phi}\left(\cos\phi \frac{\overline{v'\theta'}}{\overline{\theta}_z}\right) \tag{3}$$

where a is the radius of the Earth which is 6.37×10^6 m. $\overline{v}$ and $\overline{w}$ are the zonal-mean meridional and vertical winds. v' is the perturbation of the meridional wind from the zonal mean. ρ_0 is the atmospheric neutral density. $\overline{\theta}$ is the potential temperature and $\overline{\theta}_z = \frac{\partial \overline{\theta}}{\partial z}$. $\overline{X}_k$ is the chemical tendency due to eddy diffusion and it is defined as

$$X_K = \frac{1}{\rho_0}\frac{\partial}{\partial z}\left(\rho_0 K_{zz}\frac{\partial \mu}{\partial z}\right) \tag{4}$$

where K_{zz} is the eddy diffusion. Eddy diffusion is a parameterization for subgrid scale motions. In this model, this includes diffusion due to breaking gravity waves. $\overline{X}_d$ is the chemical tendency due to molecular diffusion, and it is defined as

$$X_D = \frac{1}{\rho_0}\frac{\partial}{\partial z}\left(\rho_0 D_\mu \frac{\partial \mu}{\partial z}\right) - \frac{1}{\rho_0}\frac{\partial}{\partial z}\left(\rho_0 \mu w_D\right) \tag{5}$$

where D_μ is the molecular diffusion for species μ and w_D is its corresponding diffusive separation velocity. For more details on this chemical tendency analysis, see Smith et al. (2011).

Equation (1) states that the time rate-of-change of a given species is driven by advection due to the residual circulation, chemical production rate, chemical loss, K_{zz}, and molecular diffusion. The production sources of CO_2 in the MLT region are negligible so the production rate can be ignored.

In the MLT region, the most important chemical reactions of CO_2 are photodissociation reactions. Photodissociation of CO_2 in the MLT region is due to UV and EUV radiation (Solomon & Brasseur, 1986). Both wavelengths induce the same reaction:

$$L : CO_2 + h\nu \rightarrow CO + O \tag{6}$$

Reaction L involves the production of carbon monoxide and atomic oxygen. Below 90 km, photodissociation of CO_2 is driven more by UV radiation. Above 90 km, photodissociation of CO_2 is driven more by EUV radiation (Garcia et al., 2014).

Equation (1) determines the relative contribution (in ppm/d) of chemical reactions and transport processes to the changes in a given species. It does not, however, determine which of these processes are important for a given time scale. For chemical reactions, this is best determined by the species chemical lifetime, which is given by

$$\tau_{\text{chem}} = \frac{1}{\overline{L}} \tag{7}$$

where L is the photochemical loss rate. For transport processes, this is best determined by the transport time scales. For meridional and vertical advection due to the residual circulation, these are given by

$$\tau_{v^*} = \frac{l}{v^*} \tag{8}$$

$$\tau_{w^*} = \frac{\overline{H_\mu}}{w^*} \tag{9}$$

where l is a characteristic meridional length which this work sets as 10° or ~1,000 km (Jones et al., 2016). $\overline{H_\mu}$ is the species scale height. For mixing due to eddy and molecular diffusion, these are given by

$$\tau_{K_{zz}} = \frac{\overline{H_\mu}^2}{K_{zz}} \tag{10}$$

$$\tau_D = \frac{\overline{H_\mu}^2}{D} \tag{11}$$

Given a certain time span, the most important chemical reactions and transport processes are those whose time scales are less than the given time span. Also, a given species is chemically inert over a certain time span if its photochemical lifetime is much longer than its transport time scale.

2.3. Multiple Linear Regression and Correlation Analysis

All of the parameters calculated from the observations and model outputs are subject to a multiple linear regression (MLR) to determine the SC dependencies of these parameters. *F* test is used to determine the statistical significance of the fits. This approach is similar to Gan et al. (2017), who performed an MLR on temperature and the terms of the thermodynamic equation, namely, advection of temperature, adiabatic heating, and diabatic heating. This work focuses on the SC response in June. Hence, an MLR is applied to all time series of the parameters in June. The time series of the parameters are fitted into this equation:

$$\mu = A + Bt + C\times F10.7 + D\times \mathrm{QBO} + E\times \mathrm{MEI} \tag{12}$$

Here *A* is the mean. *B* is the linear trend. *C* is the regression coefficient for SC. SC is represented by the F10.7 index. *D* is the regression coefficient for the quasi-biennial oscillation (QBO) which is represented by the 30-mb QBO index. *E* is the regression coefficient for the El Niño–Southern Oscillation (ENSO) which is represented by the multivariate ENSO index (MEI). For example, all CO_2 concentrations in June for all years were collected, and the MLR fitting shown in equation (12) was conducted to obtain coefficients of F10.7, QBO, and MEI terms. This work only shows the SC responses in June to ensure that influences of the sudden stratospheric warming are not aliased into the results (Cullens et al., 2016; Gan et al., 2017; Liu & Roble, 2002). This allows us to establish a baseline dynamic for the SC response of the MLT region during the dynamically active winter season. This work will not attempt to show the evolution of the MLT's SC response over a given season because this work does a bimonthly averaging on all observed, modeled, and derived parameters.

Apart from an MLR, this work will also involve presenting the time series of some of the observed, modeled, or derived parameters. The temporal mean of the time series will be removed. Showing these residual time series will help confirm the MLR coefficients. This will include doing a correlation analysis where the condition for statistical significance is for *p*-value less than 0.05. Comparing the actual time series with the results of an MLR and correlation analysis will present some insights on the frequent application of these methods to SC studies.

The flow of our analysis is as follows. First, the SC response of the observed and modeled CO_2 in June is compared. Specifically, SABER CO_2 from 2002 to 2015 is compared with SD-WACCM CO_2 from 2002 to 2014. This is done to validate SD-WACCM CO_2. After validating SD-WACCM, the SC response of CO_2 in June over the winter hemisphere as modeled by SD-WACCM from 1979 to 2014 is presented. To diagnose the SC response of CO_2 in the model, the SC response of the photochemical and transport tendency terms is determined. In conjunction, the SC response of the residual meridional velocity, residual vertical velocity, eddy diffusion (K_{zz} hereafter), and molecular diffusion coefficients are also determined. Finally, since the residual circulation and the diffusion processes in the MLT region are predominantly driven by wave-mean flow dynamics, the SC responses of the zonal-mean zonal wind and gravity wave drag are determined. Strictly speaking, planetary waves and tides are also important in the middle atmosphere. They are not analyzed here because the residual circulation and K_{zz} in the MLT region are driven primarily by gravity waves. Also, an analysis involving these planetary-scale waves will require looking at each type of wave. This is beyond the scope of this paper.

3. Results

In this section, we first compare the observed and modeled SC responses of CO_2. This will determine how well SD-WACCM models these observed SC responses. Then, the SC responses of CO_2 in June over the winter hemisphere as modeled by SD-WACCM from 1979 to 2014 are presented and explained. Finally, the SC

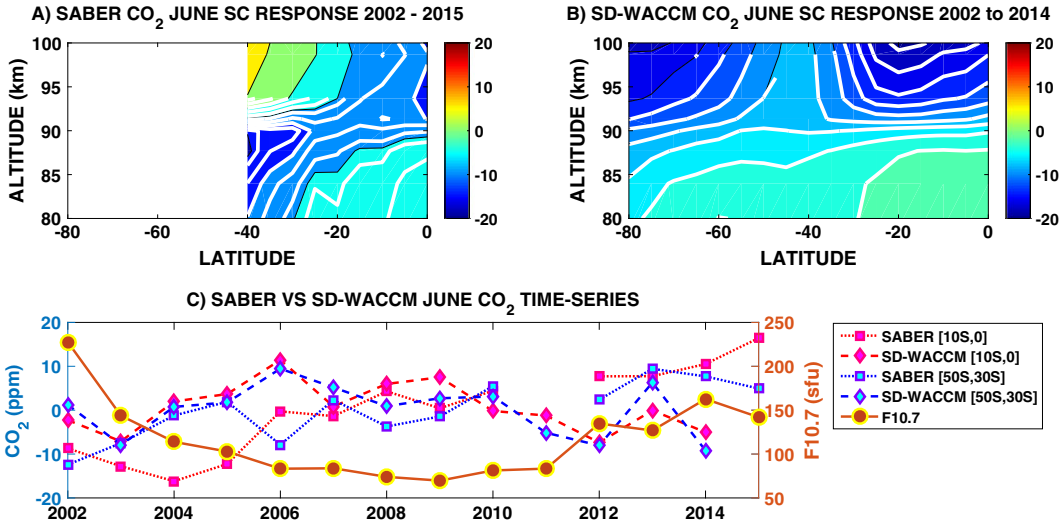

Figure 1. Regression coefficients between CO_2 residual and F10.7 index as a function of altitude and latitude. (a) Coefficients for F10.7 from multiple linear regression (MLR) fitting to Sounding of the Atmosphere using Broadband Emission Radiometry (SABER) CO_2 residual in June from 2002 to 2015. (b) Coefficients for F10.7 from MLR fitting to Specified Dynamics-Whole Atmosphere Community Climate Model (SD-WACCM) CO_2 residual in June from 2002 to 2014. The white lines denote regions of statistical significance for p-value >90%. (c) Time series of SABER and SD-WACCM CO_2 residual in June from 2002 to 2015 averaged between altitudes 95 and 100 km. Figure legend indicates latitudinal coverage.

responses of residual circulation, K_{zz}, zonal-mean zonal wind, zonal-mean temperature, and gravity wave drag are presented and related to the SC responses of CO_2. All figures comprise 3 to 4 subplots. Each subplot will be denoted as Figures x and y, where x is the figure number and y is the subplot letter.

3.1. Comparison of SABER CO_2 and SD-WACCM CO_2

The SC response of SABER CO_2 in June between altitudes 80 and 100 km from 2002 to 2015 as regression coefficients for F10.7 is shown in Figure 1a. Similarly, the SC response of SD-WACCM CO_2 between altitudes 80 and 100 km in June from 2002 to 2014 as regression coefficients for F10.7 is shown in Figure 1b. Below 85 km, both SABER and SD-WACCM have statistically significant weak positive responses with regression coefficients of around +5 ppm/100 sfu between 30°S and the equator. A positive response indicates that during solar maximum, there is an increase in CO_2. Both SABER and SD-WACCM also have statistically significant negative responses with regression coefficients of around −8 ppm/100 sfu poleward of 30°S. These regression coefficients below 85 km translate to less than ±1% change from solar minimum to solar maximum. Above 85 km, both SABER and SD-WACCM have statistically significant negative response over latitudes 30°S to 0. A negative response indicates that during solar maximum, there is a decrease in CO_2. However, SD-WACCM has regression coefficients of at least −15 ppm/100 sfu in this region, while SABER only has regression coefficients of no more than −10 ppm/100 sfu. These regression coefficients above 85 km correspond to at least −5% change from solar minimum to solar maximum. Southward of this region, the responses are not statistically significant for both SABER and SD-WACCM.

To confirm these regression coefficients, Figure 1c shows a time series of June data points over two regions. Only the temporal mean was removed from these time series. These time series are overlaid with the F10.7 index. The first region is the region where both SABER and SD-WACCM show statistically significant negative responses above 95 km between latitude 10°S and the equator. For periods when the F10.7 index is greater than 150 sfu, both SABER and SD-WACCM show magnitudes below average. For periods when the F10.7 index is below 90 sfu, both SABER and SD-WACCM show magnitudes above average. The second region is the region where both SABER and SD-WACCM show nonstatistically significant positive responses and this is above 95 km between latitude 50°S and 30°S. It can be seen that positive and negative anomalies are present at both F10.7 extremes. These time series support the regression coefficients of Figures 1a and 1b. These similarities in SABER and SD-WACCM give us confidence in utilizing the full length of SD-WACCM outputs for a more in-depth analysis of the SC response of CO_2 in the MLT region. So far, only Emmert et al. (2012) have

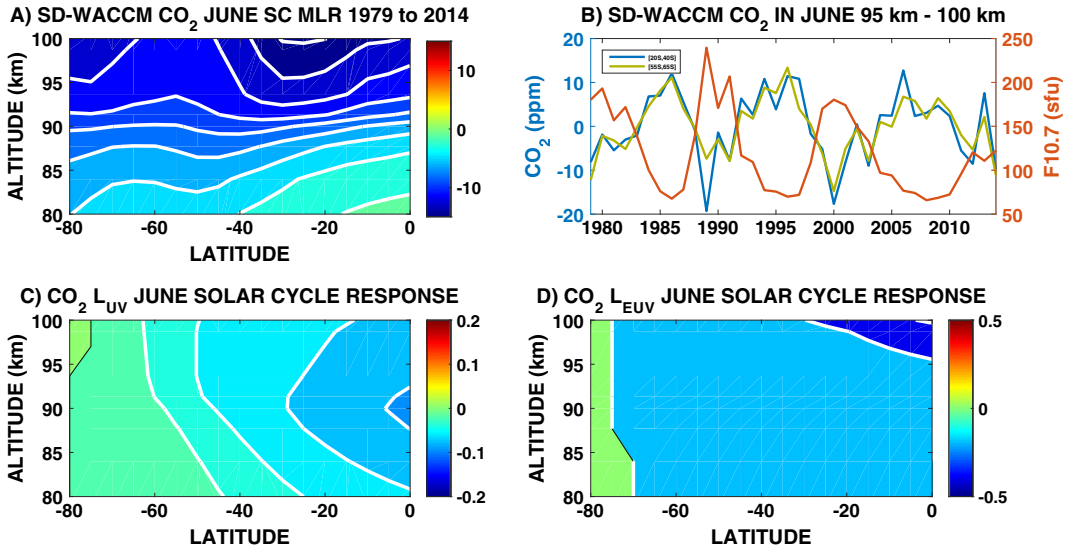

Figure 2. (a) Regression coefficients (in ppm/100 sfu) between Specified Dynamics-Whole Atmosphere Community Climate Model (SD-WACCM) CO_2 residual and the F10.7 index in June from 1979 to 2014. (b) Time series of SD-WACCM CO_2 residual averaged between altitudes 95 and 100 km. Figure legend indicates latitudinal coverage. (c) Regression coefficients (in ppm/d/100 sfu) between L_{UV} term and F10.7 index in June from 1979 to 2014. (d) Regression coefficients (in ppm/d/100 sfu) between L_{EUV} term and F10.7 index in June from 1979 to 2014. See text for details. The white lines denote regions of statistical significance for *p*-value >90%.

presented the SC variation of CO_2. Using CO_2 measurements from the Atmospheric Chemistry Experiment Fourier Transform Spectrometer, they showed that global-mean CO_2 has a negative SC response due to photodissociation by EUV and UV radiation.

3.2. Solar Cycle Response of CO_2 Over the Austral Winter MLT Region

Figure 2a shows the SC response of SD-WACCM CO_2 in June from 1979 to 2014. This plot shows that CO_2 is consistently lower during solar maximum. This work will focus on the responses over two regions. The first region is above 90 km between latitudes 40°S and 20°S where there are peak regression coefficients of at least −10 ppm/100 sfu (referred to as strong region hereafter). The second region is the region above 90 km and between 65°S and 55°S, where the lowest regression coefficients of around −5 ppm/100 sfu occur (referred to as weak region hereafter). Figure 1b also exhibited similar characteristics even if it only utilized data that is one solar cycle long. This suggests that from 2002 to 2015, the SC has the most dominant interannual variation of MLT CO_2 in June.

To confirm these regression coefficients, Figure 2b shows a time series of June data points from 1979 to 2014 over strong and weak regions. Only the temporal mean is removed. These time series are overplotted with the F10.7 index. The time series of strong region clearly shows the anticorrelation between SD-WACCM CO_2 in this region and the F10.7 index. In addition, the years of local maximum have the following magnitudes: +12.08 ppm in 1986, +11.4 ppm in 1996, +12.73 ppm in 2006, and + 7.57 ppm in 2013. The years of local minimum have the following values: −8.145 ppm in 1979, −19.31 ppm in 1989, and −17.67 ppm in 2000. The time series of weak region also clearly shows the anticorrelation between SD-WACCM CO_2 in this region and the F10.7 index. However, the years of local maximum have the following magnitudes: +11.16 ppm in 1986, +13.28 ppm in 1996, +7.18 ppm in 2006, and +3.3 ppm in 2013. The years of local minimum have the following magnitudes: −11.45 ppm in 1979, −10.23 ppm in 1989, and −15.02 ppm in 2000. The time series show that, from a strictly numerical perspective, the stronger regression coefficients over the strong region are correct. It further shows that the SC is the strongest interannual variation of lower thermospheric CO_2 in June.

To explain the SC response of SD-WACCM CO_2 in June, the SC response of its most important chemical loss reactions in the MLT region is first presented. SD-WACCM accounts for the two most important chemical loss

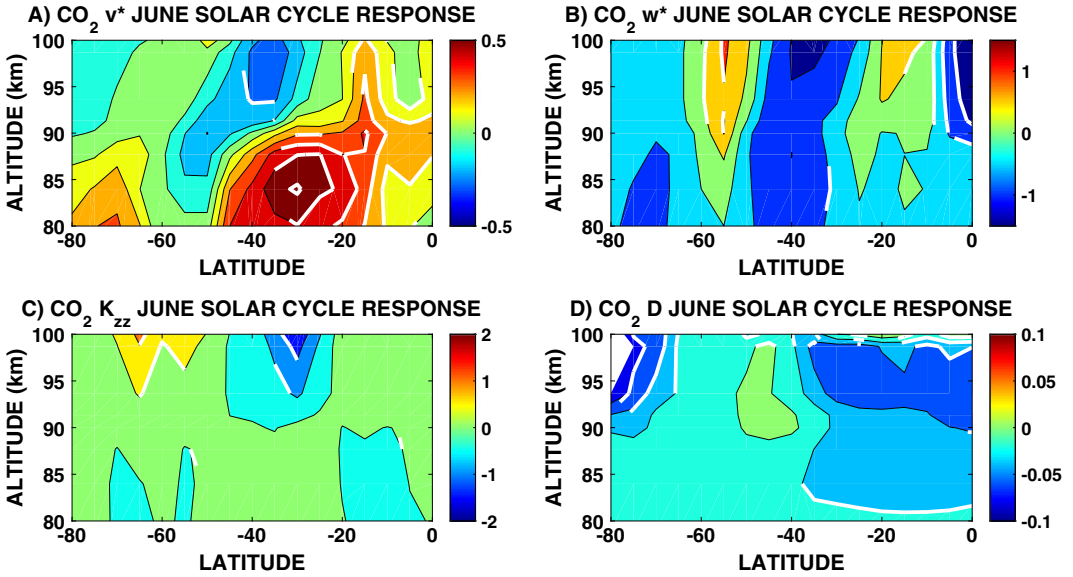

Figure 3. (a) Coefficients for F10.7 for the multiple linear regression (MLR) fitting of the transformed Eulerian mean (TEM) meridional transport term. (b) Coefficients for F10.7 for the MLR fitting of the TEM vertical transport term. (c) Coefficients for F10.7 for the MLR fitting of eddy diffusion term. (d) Coefficients for F10.7 for the MLR fitting of molecular diffusion term. Units are all ppm/d/100 sfu. The white lines denote regions of statistical significance for *p*-value >90%.

reactions of CO_2 in the MLT region. Both reactions involve the photodissociation of CO_2 and yield the same products, as given in equation (6), but are driven by radiation at different wavelengths of the solar spectrum. Below 95 km, the photodissociation of CO_2 is predominantly driven by UV radiation. L_{UV} gives the chemical tendency of this reaction. Figure 2c shows the SC response of L_{UV} in June from 1979 to 2014. It shows a peak negative response with regression coefficients of around −0.1 ppm/100 sfu between 85 and 95 km over the equator. The response weakens with increasing latitude. The absolute magnitude of L_{UV} is negative since it is a photochemical loss reaction and always acts to reduce CO_2. The negative response of L_{UV} to the SC therefore indicates that more CO_2 is lost during solar maximum as a result of L_{UV}. This implies that this reaction intensifies during solar maximum. This is consistent with how UV fluxes vary 3–10% throughout a SC (Ermolli et al., 2013; Haberreiter et al., 2017).

Above 95 km, the photodissociation of CO_2 is predominantly driven by EUV radiation (Garcia et al., 2014). L_{EUV} gives the chemical tendency of this reaction. Figure 2d shows the SC response of L_{EUV} in June from 1979 to 2014. It shows a peak negative response with regression coefficients of around −0.5 ppm/100 sfu above 95 km over the equator. Similar to L_{UV}, this indicates that more CO_2 is lost during solar maximum as a result of reaction L_{EUV}. The SC response of L_{EUV} also weakens with increasing latitude. Figure 2a shows peak negative responses above 95 km. This shows that L_{EUV} is more important than L_{UV} in explaining the SC response of CO_2 above 95 km. This is consistent with how the EUV fluxes vary with a factor of 2 or more with 11-year SC (Lean et al., 1997).

Figure 2a clearly shows that the SC response of CO_2 is negative throughout the MLT region. Both L_{UV} and L_{EUV} also show the same characteristic. This shows that these photochemical loss reactions contribute to the general negative response of CO_2 throughout the MLT region. However, the presence of strong and weak regions cannot solely be explained by photochemical loss reactions. This prompts us to look into the transport processes.

The transport of CO_2 is driven by the TEM residual circulation, K_{zz}, and molecular diffusion. The TEM residual circulation is composed of the meridional residual velocity (v^*) and the vertical residual velocity (w^*). The term $-\frac{\overline{v}^*}{a}\frac{\partial\overline{\mu}}{\partial\phi}$ in equation (1) is thus the meridional advection of a given tracer species, while $-\overline{w}^*\frac{\partial\overline{\mu}}{\partial z}$ is the vertical advection of a given tracer species. Figure 3a shows the SC response of the meridional advection of CO_2 (v^*_{CO2} hereafter) in June from 1979 to 2014. There is a statistically significant positive response below 90 km

between latitudes 50°S and 20°S with regression coefficients of around 0.5 ppm/d/100 sfu. A positive response indicates that during solar maximum, v^*_{CO2} increases CO_2. Above 90 km, there is also a statistically significant positive response between latitudes 20°S and the equator. In addition, there is a statistically significant negative response over 40°S. A negative response indicates that during solar maximum, v^*_{CO2} decreases CO_2.

Figure 3b shows the SC response of the vertical advection of CO_2 (w^*_{CO2} hereafter) in June from 1979 to 2014. The statistically significant responses are mostly situated above 95 km. There is a statistically significant positive response over two regions. A positive response indicates that during solar maximum, w^*_{CO2} increases CO_2. The first region with statistically significant positive response above 95 km is between latitudes 30°S and 10°S, while the second region with statistically significant positive response above 95 km is between latitudes 60°S and 40°S. Both regions have regression coefficients of around +1 ppm/100 sfu. The only region with a statistically significant negative response above 95 km is over the equator. It has regression coefficients of around −1.5 ppm/100 sfu. There is a peak negative response above 95 km between latitudes 50°S and 30°S, but it is not statistically significant. A negative response indicates that during solar maximum, w^*_{CO2} decreases CO_2.

The statistically significant positive SC response of w^*_{CO2} above 95 km between latitudes 60°S and 40°S in Figure 3b coincides with weak region. This suggests that w^*_{CO2} could be behind the weak region by counteracting the SC response of the photochemical reactions.

Apart from these advection processes, diffusion processes are also important in the transport of CO_2. In the MLT region, the most important diffusion processes are K_{zz} and molecular diffusion. Specifically, K_{zz} acts to transport CO_2 upward, while molecular diffusion acts to transport CO_2 downward (Smith et al., 2011). Thus, the K_{zz} tendency of CO_2 ($K_{zz,\ CO2}$ hereafter) indicates the amount of CO_2 being transported by K_{zz} into a given region via upward transport. An increase in $K_{zz,\ CO2}$ indicates an increase in CO_2 and vice versa. The molecular diffusion tendency of CO_2 (D_{CO2} hereafter) indicates the amount of CO_2 being removed by molecular diffusion into a given region via downward transport. An increase in D_{CO2} indicates a decrease in CO_2.

Figure 3c shows the SC response of $K_{zz,\ CO2}$ in June from 1979 to 2014. Above 90 km, there is a statistically significant negative response with regression coefficients of around −1 ppm/100 sfu between latitudes 50°S and 20°S, while there is a statistically significant positive response with regression coefficients of around +1 ppm/100 sfu between latitudes 70°S and 50°S. A positive response indicates that during solar maximum, more CO_2 is transported into a region by K_{zz}, while the opposite holds for a negative response. Figure 3d shows the SC response of D_{CO2} in June from 1979 to 2014. D_{CO2} has statistically significant positive responses with regression coefficients of around +0.08 ppm/d /100sfu above 98 km between latitude 40S and the equator. There are statistically significant negative responses with regression coefficients of around −0.05 ppm/d/100 sfu between altitudes 90 and 100 km over latitudes 80°S to 60°S.

The statistically significant positive and negative responses of $K_{zz,\ CO2}$ coincide with weak and strong regions, respectively. This suggests that K_{zz} may also be as important as vertical advection in fully explaining the SC response of CO_2 in the MLT region. This can be checked by comparing the time scales of these transport processes. Figure 4a shows the vertical profile of the time scales of the chemical reactions and transport processes averaged between 65°S and 55°S. This plot helps explain the weak region. It shows that above 95 km, the transport time scales of K_{zz} and vertical advection are both less than 10 days. Figure 4b shows the vertical profile of the time scales of the chemical reactions and transport processes averaged between 40°S and 20°S. This plot helps explain the strong region. It shows that above 90 km, the time scales of both K_{zz} and vertical advection are less than 100 days. This work deals with the SC, which has a time scale longer than these time scales. Therefore, these time scales support the argument that both vertical advection and K_{zz} are important in the SC response of lower thermospheric CO_2.

3.3. Solar Cycle Response of Austral Winter MLT Dynamics

It has now been shown that the SC responses of CO_2 in June require both photochemistry and transport. Specifically, transport by K_{zz} and vertical advection are both important in driving the SC response of CO_2. However, an analysis of the transport tendency terms only determines whether a given transport term is important. In this section, we look into the causes of the SC response of the transport terms.

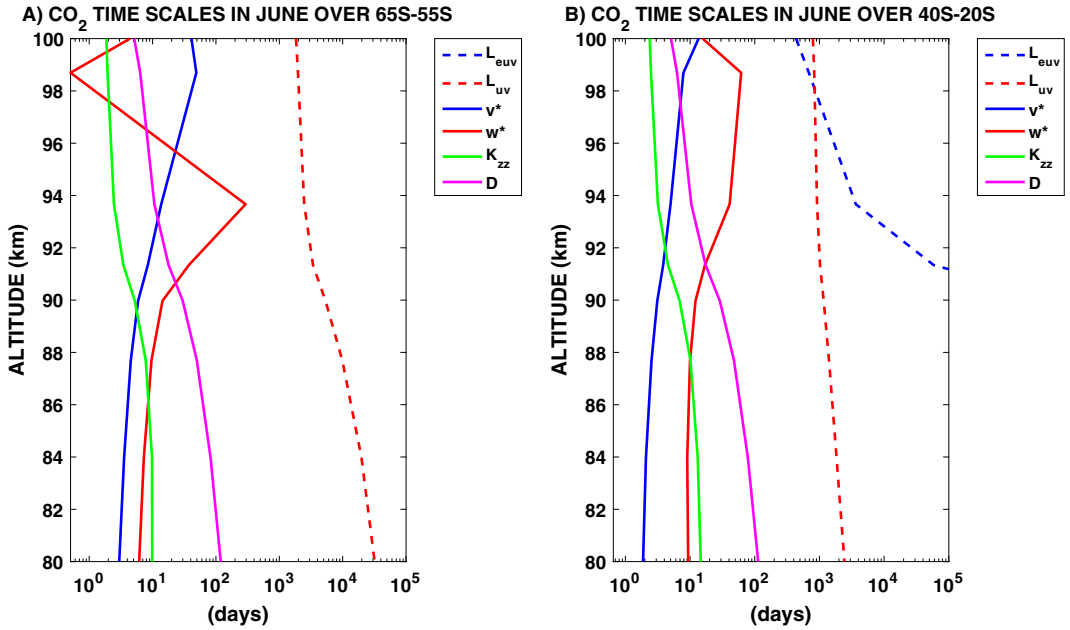

Figure 4. (a) CO_2 time scales (in days) averaged between latitudes 65°S and 55°S as a function of altitude. (b) CO_2 time scales (in days) averaged between latitudes 40°S and 20°S as a function of altitude. Figure legend indicates chemical reaction or transport process.

Figure 5a shows the SC response of SD-WACCM v^* and w^* in June from 1979 to 2014 as wind vectors. The v^* and w^* used for these plots are their regression coefficients with the F10.7 index. Strictly speaking, regression coefficients are not vectors. However, this vector plot was compared with a contour plot of the actual regression coefficients, and they were consistent. Thus, to save figure space, this work presents the regression coefficients as wind vectors. This is overplotted by the SC response of CO_2 in June between altitudes 80 and 100 km. The plot shows that above 95 km, weak region coincides with a region wherein the residual circulation has statistically significant enhanced upwelling during solar maximum. However, strong region coincides with a region, wherein the residual circulation does not have any statistically significant SC response.

Below 80 km, the residual circulation exhibits a statistically significant poleward and downward circulation during solar maximum. The downwelling occurs between altitudes 60 and 80 km over latitudes 50°S to 40°S. This SC response in the mesospheric residual circulation is consistent with the suggested SC response of the residual circulation in WACCM4 and Extended Canadian Middle Atmosphere Model (Cullens et al., 2016; Gan et al., 2017). This work adds to our knowledge by showing how recently suggested SC response of the mesospheric residual circulation occurs simultaneously with the suggested SC response of the lower thermospheric residual circulation.

Figure 5b shows the SC response of SD-WACCM K_{zz} in June from 1979 to 2014. Above 95 km, there is a statistically significant SC response in K_{zz} with regression coefficients of around -15 $m^2/s/100$ sfu between latitudes 40°S and 20°S. This indicates that during solar maximum, K_{zz} is reduced. Meanwhile, also above 95 km, there is a statistically significant positive SC response in K_{zz} with regression coefficients of around $+10$ $m^2/s/100$ sfu between latitudes 70°S and 40°S. This indicates that during solar maximum, K_{zz} is increased in this region. These regions of positive and negative SC responses in K_{zz} coincide with weak and strong regions, respectively. Figures 5a and 5b therefore show that enhanced upwelling and increased K_{zz} during solar maximum contribute to the weak region while only decreased K_{zz} during solar maximum contributes to the strong region.

It has now been clear that the SC response of MLT CO_2 in the MLT region is influenced by the SC responses of the residual circulation and K_{zz}. We now complete the picture by explaining these SC changes in the residual circulation and K_{zz}. This is done by looking into the SC responses of wave-mean flow dynamics. Specifically, we present the SC response of zonal wind and gravity wave drag.

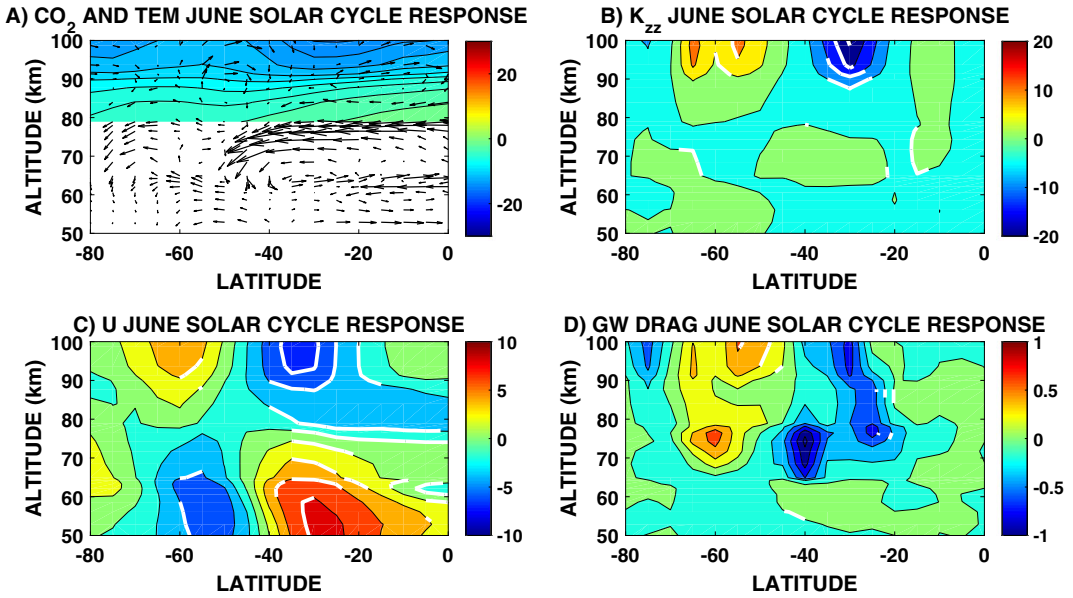

Figure 5. Regression coefficients for F10.7 index as a function of altitude and latitude. (a) Coefficients for F10.7 for the multiple linear regression (MLR) fitting of Specified Dynamics-Whole Atmosphere Community Climate Model CO_2 residual as filled contour. Overplotted is the residual circulation wind vectors. Meridional wind ranges between −0.5 and 0.5 m/s, while vertical wind ranges between −2 and 2 m/s. Vertical wind though is multiplied by 100 in the plots. (b) Coefficients for F10.7 for the MLR fitting of the eddy diffusion coefficients. (c) Coefficients for F10.7 for the MLR fitting of zonal wind. (d) Coefficients for F10.7 for the MLR fitting of gravity wave drag multiplied by 1,000. The unit of subplots a and b is m/s/100 sfu. The unit of subplot c is m^2/s/100 sfu. For subplot a, refer to Figure 2a for clearer look at statistically significant regions. For subplots b to d, the white lines denote regions that are statistically significant for *p*-value >90%.

Figure 5c shows the SC response of SD-WACCM zonal-mean zonal wind (*U*) in June from 1979 to 2014. Below 80 km, there is a statistically significant positive SC response with regression coefficients of around +6 m/s/100 sfu between 40°S and 20°S. A positive SC response in *U* indicates that during solar maximum, westerly zonal winds are getting stronger while easterly zonal winds are getting weaker. Then there is a statistically significant negative SC response with regression coefficients of around −5 m/s/100 sfu between 60°S and 40°S. A negative SC response in *U* indicates that during solar maximum, westerly zonal winds are getting weaker while easterly zonal winds are getting stronger. Kodera and Kuroda (2002) explained that the positive SC response of *U* below 80 km in early winter is due to an increase in the temperature gradient, while the negative SC response is due to the poleward refraction of planetary waves. From 80 to 100 km, there is a negative response with regression coefficients of around −7 m/s/100 sfu between 40°S and 20°S, while there is a positive response with regression coefficients of around +3 m/s/100 sfu between 60°S and 40°S. The positive response in *U* below 80 km along with the Coriolis force has been shown to explain the net poleward and downward residual circulation SC response in this region (Cullens et al., 2016; Gan et al., 2017).

Figure 5d shows the SC response of SD-WACCM gravity wave drag that is due to specified gravity waves ($\overrightarrow{F}_{gw}$) in June from 1979 to 2014. Above 70 km, there are negative responses with regression coefficients of around −0.5e−4 m/s^2/100 sfu between 40°S and 20°S. This indicates that during solar maximum, there is an increase in easterly gravity wave drag. However, the only statistically significant regions are between 80 and 90 km over 30°S to 20°S. There are also positive responses with regression coefficients of around +0.5e−4 m/s^2/100 sfu between 60°S and 40°S. This indicates that during solar maximum, there is an increase in westerly gravity wave drag. The only statistically significant regions are above 90 km. While there are minimal regions of statistical significance, Figures 5c and 5d show that these SC responses in $\overrightarrow{F}_{gw}$ could clearly explain the SC responses in *U*. Regions where there is an increase in westerly gravity wave drag in solar maximum coincide with a westerly zonal-wind anomaly. Also, regions where there is an increase in easterly gravity wave drag also coincide with an easterly zonal-wind anomaly.

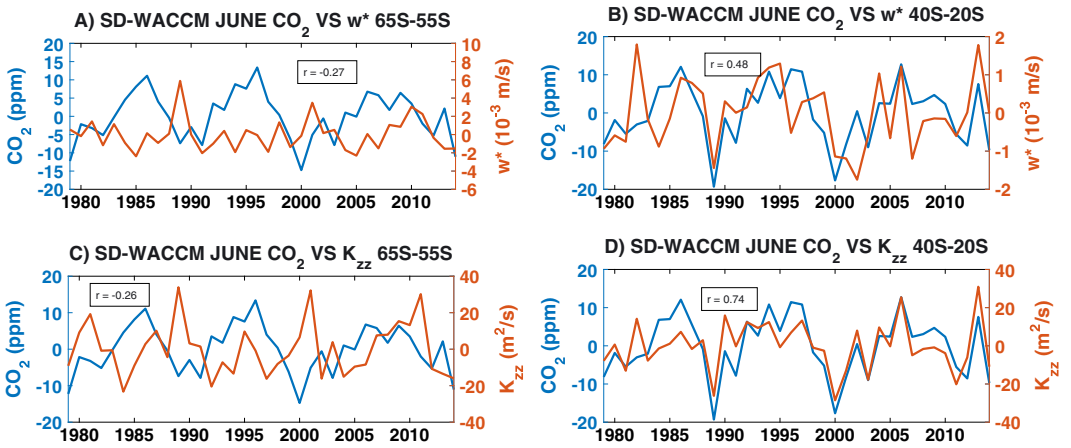

Figure 6. (a) Time series of Specified Dynamics-Whole Atmosphere Community Climate Model (SD-WACCM) CO_2 and w^* averaged between altitudes 95 and 100 km and between latitudes 65°S and 55°S. (b) Time series of SD-WACCM CO_2 and w^* averaged between altitudes 95 and 100 km and between latitudes 40°S and 20°S. (c) Time series of SD-WACCM CO_2 and K_{zz} averaged between altitudes 95 and 100 km and between latitudes 65°S and 55°S. (d) Time series of SD-WACCM CO_2 and K_{zz} averaged between altitudes 95 and 100 km and between latitudes 40°S and 20°S. Each subplot includes the correlation coefficient.

To confirm and assess these regression coefficients, Figures 6a and 6b show the time series of CO_2 and w^* in June from 1979 to 2014 over the weak and strong regions, respectively while Figures 6c and 6d show the time series of CO_2 and K_{zz} in June from 1979 to 2014 also over the weak and strong regions. Only the temporal mean was removed from the time series. The correlation coefficients (r) are also given. Recall that Figure 2 b has already shown how well anticorrelated these time series of CO_2 are with the F10.7 index. Figures 6a and 6b show that w^* is correlated with CO_2 over the strong region with a correlation coefficient of 0.48 that is statistically significant at p-value less than 0.05. Figures 6c and 6d show that K_{zz} is also only correlated with CO_2 over the strong region with a correlation coefficient of 0.74 that is statistically significant. However, even if the correlation coefficient between K_{zz} and CO_2 over the weak region is only -0.26 and not statistically significant at p-value less than 0.05, the time series does show significant enhancements in K_{zz} only during solar maximum years. w^* also shows similar enhancements during solar maximum years, but these enhancements are also present in solar minimum years. This makes it doubtful whether these enhancements are indeed due to the SC.

For the weak region, these correlations suggest that during solar minimum, the weak region is solely controlled by the photodissociation reactions of CO_2. On the other hand, during solar maximum, there is a competition between photodissociation reactions and K_{zz}; that is, while photodissociation reactions are acting to reduce CO_2, K_{zz} is acting to enhance CO_2. For the strong region, these correlation coefficients add further support to the regression coefficients showing that the strong region also requires K_{zz} but disagrees with the regression coefficients that the strong region may not at all require vertical advection.

The correlation coefficients involving CO_2, w^*, and K_{zz} helped to better assess the MLR coefficients of these parameters. To also confirm and assess the MLR coefficients in U and $\overrightarrow{F}_{gw}$, Figures 7a and 7b show the time series of CO_2 and U in June from 1979 to 2014 also over the weak and strong regions. The correlation coefficients of CO_2 and U over the weak and strong regions are -0.41 and 0.74, respectively, and are both statistically significant for p-value less than 0.05. Figures 7c and 7d also show the time series of CO_2 and $\overrightarrow{F}_{gw}$ in June from 1979 to 2014 over the weak and strong regions. The correlation coefficient of CO_2 and $\overrightarrow{F}_{gw}$ over the weak region is -0.31 and is not statistically significant, while their correlation coefficients over the strong region is 0.65 and is statistically significant (p-value less than 0.05). Similar to Figures 6a and 6c, Figures 7a and 7c also show significant responses during solar maximum, while there are no clear responses during solar minimum; that is, during solar maximum, there is a westerly anomaly in both U and $\overrightarrow{F}_{gw}$, while during solar minimum, there is no clear response. This is not easy to capture using an MLR. On the other

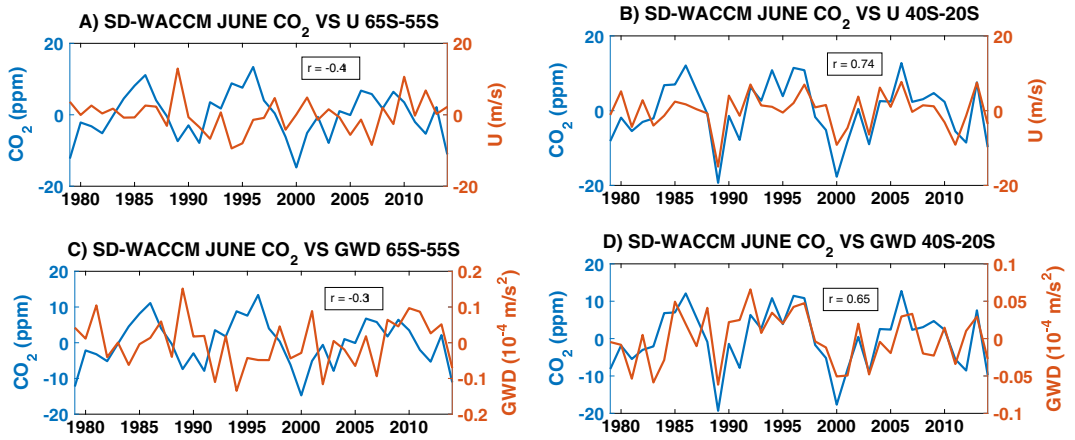

Figure 7. (a) Time series of Specified Dynamics-Whole Atmosphere Community Climate Model (SD-WACCM) CO_2 and $\overline{U}$ averaged between altitudes 95 and 100 km and between latitudes 65°S and 55°S. (b) Time series of SD-WACCM CO_2 and $\overline{U}$ averaged between altitudes 95 and 100 km and between latitudes 40°S and 20°S. (c) Time series of SD-WACCM CO_2 and $\overrightarrow{F}_{gw}$ averaged between altitudes 95 and 100 km and between latitudes 65°S and 55°S. (d) Time series of SD-WACCM CO_2 and $\overrightarrow{F}_{gw}$ averaged between altitudes 95 and 100 km and between latitudes 40°S and 20°S. Each subplot includes the correlation coefficient.

hand, Figures 7b and 7d show that there are significant responses in U and $\overrightarrow{F}_{gw}$ during solar maximum and solar minimum; that is, during solar maximum, both have an easterly anomaly while during solar minimum and both have a westerly anomaly.

Liu et al. (2017) recently showed that SABER observes an SC response in midlatitude annual mean gravity wave potential energy that is negative. Our work adds that there is also a negative SC response in gravity wave breaking and mixing between 40°S and 20°S, represented as eddy diffusion, during Austral winter. On the other hand, Jacobi (2014) showed a positive SC response in gravity wave flux over latitude 50 N during winter using ground-based observations. Our work also shows that there is a positive SC response in high-latitude gravity wave amount between 65°S and 55°S. They also used MLR to determine the SC response on their wind observations. Our work does also show a positive SC response in eddy diffusion over 50 N through an MLR. However, our time series better characterized the SC response in eddy diffusion; that is, there is an enhancement during solar maximum, but there is no clear response in solar minimum.

4. Discussion

Our work reports that these SC responses in $\overline{U}$ below 80 km also affect lower thermospheric CO_2 by modifying the lower thermospheric residual circulation and K_{zz}. Over Austral winter, the climatological $\overline{U}$ is westerly below 80 km, and it is easterly above 80 km as a result of gravity wave filtering (Andrews et al., 1987). A recent addition is that above 95 km, the climatological $\overline{U}$ in Austral winter is westerly (Qian et al., 2017; Smith et al., 2011). Similar to Cullens et al. (2016) and Gan et al. (2017), our results in Figure 5c show that during solar maximum, $\overline{U}$ below 80 km is enhanced. This drives a poleward and downward residual circulation anomaly between 50 and 80 km over the midlatitudes. The SC response of K_{zz} and $\overrightarrow{F}_{gw}$ in Figures 5b and 5d suggests that above 80 km, the enhancement in $\overline{U}$ below 80 km blocks more westerly gravity waves from propagating upward, which induces a net easterly anomaly in $\overrightarrow{F}_{gw}$ and a reduction in K_{zz}. This reduction in K_{zz} was shown to contribute to the negative SC response of CO_2. In addition, blocking more westerly gravity waves induces an easterly anomaly in $\overline{U}$ between 80 and 100 km. Above 95 km, the climatological mean of $\overline{U}$ in Austral winter is westerly. This westerly $\overline{U}$ is part of the winter-to-summer lower thermospheric residual circulation, wherein upwelling occurs over the Austral winter lower thermosphere. Our results suggest that the easterly anomaly in the region during solar maximum weakened the upwelling which caused a net downwelling in the region. This net downwelling in the region was also shown to contribute to the negative SC response of CO_2.

On the other hand, there is an easterly anomaly in $\overline{U}$ below 80 km over 60°S to 50°S shown in Figure 5c. This is consistent with Kodera and Kuroda (2002), Cullens et al. (2016), and Gan et al. (2017) where they additionally showed that this easterly $\overline{U}$ anomaly is due to anomalies in planetary wave propagation. This easterly anomaly should weaken the mesospheric easterly winter jet, which should allow more westerly gravity waves to propagate. Figures 7a and 7c clarify though that there is only a clear response above 80 km during solar maximum; that is, during solar maximum, both $\overline{U}$ and $\overrightarrow{F}_{gw}$ do show a westerly anomaly. There is no clear response during solar minimum. In addition, Figure 6c shows that this westerly anomaly coincides with an enhancement in K_{zz}. This supports the argument that the easterly anomaly in $\overline{U}$ below 80 km allows more westerly gravity waves to propagate above 80 km because an increase in westerly gravity waves will also induce an increase in K_{zz}. Our results showed that this enhancement in K_{zz} coincides with the weak region. This appears to suggest that during solar maximum, while photodissociation is acting to reduce CO_2, K_{zz} enhances CO_2.

Kodera and Kuroda (2002) actually showed that a negative anomaly in $\overline{U}$ during solar maximum occurs in middle to late winter. They showed that in early winter, $\overline{U}$ only exhibits a positive anomaly during solar maximum as a result of enhanced latitudinal gradient in temperature. The negative anomaly in $\overline{U}$ during solar maximum is a result of the eventual response of the planetary waves that begin to develop in mid to late winter. Our results show the simultaneous presence of a positive and negative anomaly in $\overline{U}$ because of our use of a bimonthly mean.

Lee et al. (2018) recently showed carbon monoxide increase during solar maximum, as observed by the Aura Microwave Limb Sounder and by WACCM 3.5 simulations. Their work showed how the residual circulation and photochemistry can drive the SC variation of CO over the winter hemisphere. Photolysis of CO_2 above ~95 km enhances the CO production during solar maximum when more UV is present for photochemistry. At the same time, this process can induce reduction of the CO_2 amount during solar maximum period. They noted though that the dynamics in the model may need to be improved to better match with observations. Peck et al. (2015) did show that the more recent WACCM4 version simulates the dynamics in the middle atmosphere better. They showed that this is indeed important in an improved modeling of the SC response of chemically active species in the middle atmosphere. Our work supports these suggestions that dynamics are indeed important in fully modeling the SC responses of both chemically active and chemically inert species in the middle atmosphere. Along with recent works by Cullens et al. (2016) and Gan et al. (2017), our work adds that there could be an SC response in dynamics that also contributes to the SC response in these species.

This is the first work to show and analyze the SC responses of lower thermospheric CO_2 in relation to the SC responses of the residual circulation and K_{zz} in the MLT region. Our confidence in these results are first hinged on how well SD-WACCM captured the general features of the SC responses of CO_2 as observed by SABER, respectively, as shown in Figures 1a and 1b. Our results are also hinged on previous works showing how well SD-WACCM models similarly complicated phenomenon in the MLT region (Chandran et al., 2014; Limpasuvan et al., 2016). Extensive global observations on the structure of the MLT region have only recently been done. Thus, long-term observations encompassing multiple SCs are still lacking. On the other hand, there are already a considerable amount of long-term observations in winds and temperature up to around 50 km. This has enabled numerical experiments with models that involve constraining the lower boundaries of these models with observations and then predicting the responses above. For example, Chandran et al. (2014) and Limpasuvan et al. (2016) have already shown that SD-WACCM can satisfactorily model the MLT response to sudden stratospheric warmings. This work provides the first prediction on the SC response of the lower thermospheric CO_2 during Austral winter.

5. Summary and Conclusions

This work utilized 13 years of SABER CO_2 data from 2002 to 2015 and 35 years of SD-WACCM model outputs from 1979 to 2014 to determine and analyze the SC response of zonal-mean CO_2 in the MLT region. MLR is used to calculate the SC response of all the parameters in this work. Correlation analysis is then done to further assess whether the MLR coefficients are indeed suggesting an apparent SC response. Results first show that SD-WACCM does reproduce the general characteristics of the SC response of SABER CO_2 in June

from 2002 to 2015. Both SD-WACCM and SABER CO_2 show that the overall SC response of CO_2 in the MLT region is negative; that is, during solar maximum, there is a decrease in CO_2. They also both show peak SC response in the tropical lower thermosphere and a general weakening of the negative SC response with increasing latitude and decreasing altitude. This gave us confidence in utilizing the full length of SD-WACCM outputs for a more in-depth analysis of the SC response of CO_2 in June.

Specified Dynamics-Whole Atmosphere Community Climate Model CO_2 in June from 1979 to 2014 shows stronger SC responses in the lower thermosphere above 95 km than in the mesosphere. This work focused on two regions. The first region called strong region is above 95 km between latitudes 40°S and 20°S where there are peak regression coefficients of at least −10 ppm/100 sfu. The second region called weak region is the region above 95 km and between 65°S and 55°S where the lowest regression coefficients of around −5 ppm/100 sfu occur. A chemical tendency analysis using the continuity equation was then done to calculate the relative contributions of the photodissociation reactions, residual circulation, K_{zz}, and molecular diffusion to these SC responses. Finally, the residual circulation velocities, K_{zz} coefficients, $\overline{U}$, and $\overrightarrow{F}_{gw}$ were shown to fully explain how wave mean-flow dynamics contribute to the SC response of CO_2 in June.

It was shown that the SC response in the weak region is due to a competition between photodissociation reactions and K_{zz}. During solar maximum, while photodissociation is acting to reduce CO_2, K_{zz} is acting to enhance it. On the other hand, the SC response in the strong region requires photodissociation reactions, vertical advection, and K_{zz}.

It was then shown that these SC responses in the photodissociation reactions, vertical advection, and K_{zz} are due to the SC response of the MLT dynamics. Specifically, it was shown that the SC response of $\overline{U}$ below 80 km is a westerly anomaly over latitudes 50°S and 40°S. Above 80 km, there is an easterly anomaly between 50°S and 40°S. There is also a decrease in K_{zz} and a net easterly anomaly in $\overrightarrow{F}_{gw}$. The SC response of $\overline{U}$, K_{zz}, and $\overrightarrow{F}_{gw}$ suggests that during solar maximum, the easterly anomaly above 80 km is a result of reduced westerly gravity waves due to the enhanced westerly $\overline{U}$ below 80 km. The decrease in K_{zz} was then shown to cause an additional forcing on the SC response of CO_2 in the strong region. In addition, it was also shown that the reduced westerly gravity waves above 80 km have an effect on the winter-to-summer lower thermospheric circulation. Westerly gravity waves are required to maintain an upwelling over the winter hemisphere. A reduction in westerly gravity waves induced a net downwelling as exhibited in the vertical velocity.

Meanwhile, the SC response of $\overline{U}$ below 80 km between 65°S and 55°S is an easterly anomaly. Above this, there is a westerly anomaly. It was shown that this westerly anomaly above 80 km between 65°S and 55°S is due to an increase in westerly gravity waves. This increase in westerly gravity waves induced an enhancement in K_{zz}, which is then shown to counteract the photodissociation reactions of CO_2. This work therefore concludes that the SC affects lower thermospheric CO_2 in Austral winter via modifications to the lower thermospheric circulation and eddy diffusion processes.

Acknowledgments

C.C.J.S. and L.C.C. are supported by grants MOST 106-2111-M-008-010 and 105-2111-M-008-001-MY3 from the Taiwan Ministry of Science and Technology. The NCU Center for Astronautical Physics and Engineering is supported by the Taiwan Ministry of Education. C.C.J.S. acknowledges the NCAR High Altitude Observatory for funding his scientific visit from June 2017 to August 2017. C.C.J.S. also acknowledges high-performance computing support from Cheyenne (doi:10.5065/D6RX99HX) provided by NCAR's Computational and Information Systems Laboratory, sponsored by the National Science Foundation. M.C.L. is supported by grant MOST 105-2111-M-001-006-MY3. J.Y. and L.Q. are supported by NASA grant NNH15ZDA001N-HSR. J.L. and D.W. are supported by NASA Sun-Climate Research at Goddard Space Flight Center. J.R. and M.M. acknowledge the SABER team. The new v2.0 SABER products presented in this paper are accessible from the SABER website: http://saber.gats-inc.com/data.php. SD-WACCM model outputs are archived on the NCAR High Performance Storage System and are available upon request. ENSO index was taken from http://www.esrl.noaa.gov/psd/enso/mei/table.html. QBO index was taken from http://www.cpc.ncep.noaa.gov/data/indices/qbo.u30.index. F10.7 was taken from http://www.spaceweather.gc.ca/solarflux/sx-5-en.php.

References

Andrews, D. G., Holton, J. R., & Leovy, C. B. (1987). *Middle atmosphere dynamics, International Geophysics Series* (Vol. 40, pp. 463–481). Orlando, FL: Academic Press.

Baldwin, M. P., & Dunkerton, T. J. (2005). The solar cycle and stratosphere-troposphere dynamical coupling. *Journal of Atmospheric and Solar-Terrestrial Physics*, *67*(1-2), 71–82. https://doi.org/10.1016/j.jastp.2004.07.018

Beig, G., Heer, J., Mlynczak, M. G., & Keckhut, P. (2008). Overview of the temperature response in the mesosphere and lower thermosphere to solar activity. *Reviews of Geophysics*, *46*, RG3002. https://doi.org/10.1029/2007RG000236

Chandran, A., Collins, R. L., & Harvey, V. L. (2014). Stratosphere-mesosphere coupling during stratospheric sudden warming events. *Advances in Space Research*, *53*(9), 1265–1289. https://doi.org/10.1016/j.asr.2014.02.005

Chiodo, G., Calvo, N., Marsh, D. R., & Garcia-Herrera, R. (2012). The 11 year solar cycle signal in transient simulations from the Whole Atmosphere Community Climate Model. *Journal of Geophysical Research*, *117*, D06109. https://doi.org/10.1029/2011JD016393

Cullens, C. Y., England, S. L., & Garcia, R. R. (2016). The 11 year solar cycle signature on wave-driven dynamics in WACCM. *Journal of Geophysical Research: Space Physics*, *121*, 3484–3496. https://doi.org/10.1002/2016JA022455

Emmert, J. T., Stevens, M. H., Bernath, P. F., Drob, D. P., & Boone, C. D. (2012). Observations of increasing carbon dioxide concentration in Earth's thermosphere. *Nature Geoscience*, *5*(12), 868–871. https://doi.org/10.1038/ngeo1626

Ermolli, I., Matthes, K., Dudok de Wit, T., Krivova, N. A., Tourpali, K., Weber, M., et al. (2013). Recent variability of the solar spectral irradiance and its impact on climate modelling. *Atmospheric Chemistry and Physics*, *13*(8), 3945–3977.

Fritts, D. C., & Alexander, M. J. (2003). Gravity wave dynamics and effects in the middle atmosphere. *Reviews of Geophysics*, *41*(1), 1003. https://doi.org/10.1029/2001RG000106

Gan, Q., Du, J., Fomichev, V. I., Ward, W. E., Beagley, S. R., Zhang, S., & Yue, J. (2017). Temperature responses to the 11 year solar cycle in the mesosphere from the 31 year (1979–2010) Extended Canadian Middle Atmosphere Model simulations and a comparison with the 14 year (2002–2015) TIMED/SABER observations. *Journal of Geophysical Research: Space Physics*, *122*, 4801–4818. https://doi.org/10.1002/2016JA023564

Garcia, R. R., López-Puertas, M., Funke, B., Marsh, D. R., Kinnison, D. E., Smith, A. K., & González-Galindo, F. (2014). On the distribution of CO2 and CO in the mesosphere and lower thermosphere. *Journal of Geophysical Research: Atmospheres*, *119*, 5700–5718. https://doi.org/10.1002/2013JD021208

Gray, L. J., Beer, J., Geller, M., Haigh, J. D., Lockwood, M., Matthes, K., et al. (2010). Solar influences on climate. *Reviews of Geophysics*, *48*, RG4001. https://doi.org/10.1029/2009RG000282

Gray, L. J., Rumbold, S. T., & Shine, K. P. (2009). Stratospheric temperature and radiative forcing response to 11-year solar cycle changes in irradiance and ozone. *Journal of the Atmospheric Sciences*, *66*(8), 2402–2417. https://doi.org/10.1175/2009JAS2866.1

Haberreiter, M., Schöll, M., Dudok de Wit, T., Kretzschmar, M., Misios, S., Tourpali, K., & Schmutz, W. (2017). A new observational solar irradiance composite. *Journal of Geophysical Research: Space Physics*, *122*, 5910–5930. https://doi.org/10.1002/2016JA023492

Hampson, J., Keckhut, P., Hauchecorne, A., & Chanin, M. L. (2005). The effect of the 11-year solar-cycle on the temperature in the upper-stratosphere and mesosphere: Part II numerical simulations and the role of planetary waves. *Journal of Atmospheric and Solar-Terrestrial Physics*, *67*(11), 948–958. https://doi.org/10.1016/j.jastp.2005.03.005

Hampson, J., Keckhut, P., Hauchecorne, A., & Chanin, M. L. (2006). The effect of the 11-year solar-cycle on the temperature in the upper-stratosphere and mesosphere—Part III: Investigations of zonal asymmetry. *Journal of Atmospheric and Solar-Terrestrial Physics*, *68*(14), 1591–1599. https://doi.org/10.1016/j.jastp.2006.05.006

Jacobi, C. (2014). Long-term trends and decadal variability of upper mesosphere/lower thermosphere gravity waves at midlatitudes. *Journal of Atmospheric and Solar-Terrestrial Physics*, *118*, 90–95. https://doi.org/10.1016/j.jastp.2013.05.009

Jones, M., Forbes, J. M., & Hagan, M. E. (2016). Solar cycle variability in mean thermospheric composition and temperature induced by atmospheric tides. *Journal of Geophysical Research: Space Physics*, *121*, 5837–5855. https://doi.org/10.1002/2016JA022701

Keckhut, P., Cagnazzo, C., Chanin, M. L., Claud, C., & Hauchecorne, A. (2005). The 11-year solar-cycle effects on the temperature in the upper-stratosphere and mesosphere: Part I—Assessment of observations. *Journal of Atmospheric and Solar-Terrestrial Physics*, *67*(11), 940–947. https://doi.org/10.1016/j.jastp.2005.01.008

Kodera, K., & Kuroda, Y. (2002). Dynamical response to the solar cycle. *Journal of Geophysical Research*, *107*(D24), 4749. https://doi.org/10.1029/2002JD002224

Kodera, K., Matthes, K., Shibata, K., Langematz, U., & Kuroda, Y. (2003). Solar impact on the lower mesospheric subtropical jet: A comparative study with general circulation model simulations. *Geophysical Research Letters*, *30*(6), 1315. https://doi.org/10.1029/2002GL016124

Kunz, A., Pan, L. L., Konopka, P., Kinnison, D. E., & Tilmes, S. (2011). Chemical and dynamical discontinuity at the extratropical tropopause based on START08 and WACCM analyses. *Journal of Geophysical Research*, *116*, D24302. https://doi.org/10.1029/2011JD016686

Labitzke, K. (2003). The global signal of the 11-year sunspot cycle in the atmosphere: When do we need the QBO? *Meteorologische Zeitschrift*, *12*(4), 209–216. https://doi.org/10.1127/0941-2948/2003/0012-0211

Langematz, U., Grenfell, J. L., Matthes, K., Mieth, P., Kunze, M., Steil, B., & Brühl, C. (2005). Chemical effects in 11-year solar cycle simulations with the Freie Universität Berlin Climate Middle Atmosphere Model with online chemistry (FUB-CMAM-CHEM). *Geophysical Research Letters*, *32*, L13803. https://doi.org/10.1029/2005GL022686

Lean, J. L., Rottman, G. J., Kyle, H. L., Woods, T. N., Hickey, J. R., & Puga, L. C. (1997). Detection and parameterization of variations in solar mid- and near-ultraviolet radiation (200–400 nm). *Journal of Geophysical Research*, *102*(D25), 29,939–29,956. https://doi.org/10.1029/97JD02092

Lee, J. N., Wu, D. L., Ruzmaikin, A., & Fontenla, J. (2018). Solar cycle variations in mesospheric carbon monoxide. *Journal of Atmospheric and Solar - Terrestrial Physics*, *170*, 21–34. https://doi.org/10.1016/j.jastp.2018.02.001

Li, T., Leblanc, T., McDermid, I. S., Keckhut, P., Hauchecorne, A., & Dou, X. K. (2011). Middle atmosphere temperature trend and solar cycle revealed by long-term Rayleigh lidar observations. *Journal of Geophysical Research*, *116*, D00P05. https://doi.org/10.1029/2010JD015275

Limpasuvan, V., Orsolini, Y. J., Chandran, A., Garcia, R. R., & Smith, A. K. (2016). On the composite response of the MLT to major sudden stratospheric warming events with elevated stratopause. *Journal of Geophysical Research: Atmospheres*, *121*, 4518–4537. https://doi.org/10.1002/2015JD024401

Lindzen, R. S. (1981). Turbulence and stress owing to gravity wave and tidal breakdown. *Journal of Geophysical Research*, *86*(C10), 9707–9714. https://doi.org/10.1029/JC086iC10p09707

Liu, H. L., & Roble, R. G. (2002). A study of a self-generated stratospheric sudden warming and its mesospheric-lower thermospheric impacts using the coupled TIME-GCM/CCM3. *Journal of Geophysical Research*, *107*(D23), 4695. https://doi.org/10.1029/2001JD001533

Liu, X., Yue, J., Xu, J., Garcia, R. R., Russell, J. M., III, Mlynczak, M., et al. (2017). Variations of global gravity waves derived from 14 years of SABER temperature observations. *Journal of Geophysical Research: Atmospheres*, *122*, 6231–6249. https://doi.org/10.1002/2017JD026604

LóPez-Puertas, M., LóPez-Valverde, M. Á., Garcia, R. R., & Roble, R. G. (2000). A review of CO2 and CO abundances in the middle atmosphere. *Atmospheric Science Across the Stratopause*, 83–100. https://doi.org/10.1029/GM123p0083

Lu, H., Gray, L. J., White, I. P., & Bracegirdle, T. J. (2017a). Stratospheric response to the 11-yr solar cycle: Breaking planetary waves, internal reflection, and resonance. *Journal of Climate*, *30*(18), 7169–7190.

Lu, H., Scaife, A. A., Marshall, G. J., Turner, J., & Gray, L. J. (2017b). Downward wave reflection as a mechanism for the stratosphere-troposphere response to the 11-yr solar cycle. *Journal of Climate*, *30*(7), 2395–2414. https://doi.org/10.1175/JCLI-D-16-0400.1

Marsh, D. R. (2011). Chemical-dynamical coupling in the mesosphere and lower thermosphere. In *Aeronomy of the Earth's atmosphere and ionosphere* (pp. 3–17). Dordrecht: Springer. https://doi.org/10.1007/978-94-007-0326-1_1

Marsh, D. R., Garcia, R. R., Kinnison, D. E., Boville, B. A., Sassi, F., Solomon, S. C., & Matthes, K. (2007). Modeling the whole atmosphere response to solar cycle changes in radiative and geomagnetic forcing. *Journal of Geophysical Research*, *112*, D23306. https://doi.org/10.1029/2006JD008306

Marsh, D. R., Mills, M. J., Kinnison, D. E., Lamarque, J. F., Calvo, N., & Polvani, L. M. (2013). Climate change from 1850 to 2005 simulated in CESM1 (WACCM). *Journal of Climate*, *26*(19), 7372–7391. https://doi.org/10.1175/JCLI-D-12-00558.1

Matthes, K., Kuroda, Y., Kodera, K., & Langematz, U. (2006). Transfer of the solar signal from the stratosphere to the troposphere: Northern winter. *Journal of Geophysical Research*, *111*, D06108. https://doi.org/10.1029/2005JD006283

Matthes, K., Langematz, U., Gray, L. L., Kodera, K., & Labitzke, K. (2004). Improved 11-year solar signal in the Freie Universität Berlin Climate Middle Atmosphere Model (FUB-CMAM). *Journal of Geophysical Research*, *109*, D06101. https://doi.org/10.1029/2003JD004012

McCormack, J. P., & Hood, L. L. (1996). Apparent solar cycle variations of upper stratospheric ozone and temperature: Latitude and seasonal dependences. *Journal of Geophysical Research*, *101*(D15), 20,933–20,944. https://doi.org/10.1029/96JD01817

Mitchell, D. M., Misios, S., Gray, L. J., Tourpali, K., Matthes, K., Hood, L., et al. (2015). Solar signals in CMIP-5 simulations: The stratospheric pathway. *Quarterly Journal of the Royal Meteorological Society*, *141*(691), 2390–2403. https://doi.org/10.1002/qj.2530

Mlynczak, M. G. (2000). A contemporary assessment of the mesospheric energy budget. In D. E. Siskind, S. D. Eckermann, & M. E. Summers (Eds.), *Atmospheric science across the stratopause, Geophys. Monogr. Ser.*, (Vol. 123, pp. 37–52). Washington, D. C.: AGU.

Pancheva, D., Mukhtarov, P., & Andonov, B. (2009). Global structure, seasonal and interannual variability of the migrating semidiurnal tide seen in the SABER/TIMED temperatures (2002–2007). *Annales Geophysicae: Atmospheres, Hydrospheres and Space Sciences*, *27*(2), 687.

Peck, E. D., Randall, C. E., Harvey, V. L., & Marsh, D. R. (2015). Simulated solar cycle effects on the middle atmosphere: WACCM3 versus WACCM4. *Journal of Advances in Modeling Earth Systems*, *7*(2), 806–822. https://doi.org/10.1002/2014MS000387

Qian, L., Burns, A., & Yue, J. (2017). Evidence of the lower thermospheric winter-to-summer circulation from SABER CO2 observations. *Geophysical Research Letters*, *44*, 10,100–10,107. https://doi.org/10.1002/2017GL075643

Randel, W. J., & Wu, F. (2007). A stratospheric ozone profile data set for 1979–2005: Variability, trends, and comparisons with column ozone data. *Journal of Geophysical Research*, *112*, D06313. https://doi.org/10.1029/2006JD007339

Rezac, L., Jian, Y., Yue, J., Russell, J. M., Kutepov, A., Garcia, R., et al. (2015a). Validation of the global distribution of CO2 volume mixing ratio in the mesosphere and lower thermosphere from SABER. *Journal of Geophysical Research: Atmospheres*, *120*, 12,067–12,081. https://doi.org/10.1002/2015JD023955

Rezac, L., Kutepov, A., Russell, J. M. III, Feofilov, A. G., Yue, J., & Goldberg, R. A. (2015b). Simultaneous retrieval of T (p) and CO2 VMR from two-channel non-LTE limb radiances and application to daytime SABER/TIMED measurements. *Journal of Atmospheric and Solar-Terrestrial Physics*, *130*, 23–42.

Richter, J. H., Sassi, F., & Garcia, R. R. (2010). Toward a physically based gravity wave source parameterization in a general circulation model. *Journal of the Atmospheric Sciences*, *67*(1), 136–156. https://doi.org/10.1175/2009JAS3112.1

Rienecker, M. M., Suarez, M. J., Gelaro, R., Todling, R., Bacmeister, J., Liu, E., et al. (2011). MERRA: NASA's modern-era retrospective analysis for research and applications. *Journal of Climate*, *24*(14), 3624–3648. https://doi.org/10.1175/JCLI-D-11-00015.1

Russell, J. M., Mlynczak, M. G., Gordley, L. L., Tansock, J. J., & Esplin, R. W. (1999). Overview of the SABER experiment and preliminary calibration results. In *Optical Spectroscopic Techniques and Instrumentation for Atmospheric and Space Research III* (Vol. 3756, pp. 277–289). International Society for Optics and Photonics.

Schmidt, H., & Brasseur, G. P. (2006). The response of the middle atmosphere to solar cycle forcing in the Hamburg Model of the Neutral and Ionized Atmosphere. *Space Science Reviews*, *125*(1–4), 345–356.

Schmidt, H., Brasseur, G. P., Charron, M., Manzini, E., Giorgetta, M. A., Diehl, T., et al. (2006). The HAMMONIA chemistry climate model: Sensitivity of the mesopause region to the 11-year solar cycle and CO2 doubling. *Journal of Climate*, *19*(16), 3903–3931. https://doi.org/10.1175/JCLI3829.1

Shibata, K., & Kodera, K. (2005). Simulation of radiative and dynamical responses of the middle atmosphere to the 11-year solar cycle. *Journal of Atmospheric and Solar-Terrestrial Physics*, *67*(1-2), 125–143. https://doi.org/10.1016/j.jastp.2004.07.022

Shindell, D., Rind, D., Balachandran, N., Lean, J., & Lonergan, P. (1999). Solar cycle variability, ozone, and climate. *Science*, *284*(5412), 305–308. https://doi.org/10.1126/science.284.5412.305

Smith, A. K., Garcia, R. R., Marsh, D. R., & Richter, J. H. (2011). WACCM simulations of the mean circulation and trace species transport in the winter mesosphere. *Journal of Geophysical Research*, *116*, D20115. https://doi.org/10.1029/2011JD016083

Solomon, S., & Brasseur, G. (1986). *Aeronomy of the middle atmosphere* (Vol. 430). Dordrecht, Boston, Lancaster & Tokyo: D. Reidel Publishing Company.

Tsutsui, J., Nishizawa, K., & Sassi, F. (2009). Response of the middle atmosphere to the 11-year solar cycle simulated with the Whole Atmosphere Community Climate Model. *Journal of Geophysical Research*, *114*, D02111. https://doi.org/10.1029/2008JD010316

Woods, T. N., & Rottman, G. J. (1997). Solar Lyman α irradiance measurements during two solar cycles. *Journal of Geophysical Research*, *102*(D7), 8769–8779. https://doi.org/10.1029/96JD03983

Zhang, X., Forbes, J. M., Hagan, M. E., Russell, J. M., Palo, S. E., Mertens, C. J., & Mlynczak, M. G. (2006). Monthly tidal temperatures 20–120 km from TIMED/SABER. *Journal of Geophysical Research*, *111*, A10S08. https://doi.org/10.1029/2005JA011504